Weak localization as a probe of spin-orbit-induced spin-split bands in bilayer graphene proximity coupled to WSe_2

E. Icking,[1,2] F. Wörtche,[1] A.W. Cummings,[3] A. Wörtche,[1] K. Watanabe,[4] T. Taniguchi,[5] C. Volk,[1,2] B. Beschoten,[1,*] and C. Stampfer[1,2]

[1] *JARA-FIT and 2nd Institute of Physics, RWTH Aachen University, 52074 Aachen, Germany*

[2] *Peter Grünberg Institute (PGI-9), Forschungszentrum Jülich, 52425 Jülich, Germany*

[3] *Catalan Institute of Nanoscience and Nanotechnology (ICN2), CSIC and BIST, Campus UAB, Bellaterra, 08193 Barcelona, Spain*

[4] *Research Center for Electronic and Optical Materials, National Institute for Materials Science, 1-1 Namiki, Tsukuba 305-0044, Japan*

[5] *International Center for Materials Nanoarchitectonics, National Institute for Materials Science, 1-1 Namiki, Tsukuba 305-0044, Japan*

(Received 13 July 2025; revised 19 January 2026; accepted 13 February 2026; published 10 April 2026)

Proximity coupling of bilayer graphene (BLG) to transition metal dichalcogenides (TMDs) offers a promising route to engineer gate-tunable spin-orbit coupling (SOC) while preserving BLG's exceptional electronic properties. This tunability arises from the layer-asymmetric electronic structure of gapped BLG, where SOC acts predominantly on the layer in contact with the TMD. Here, we present a high-quality BLG/WSe_2 device with a proximity-induced SOC gap and excellent electrostatic control. Operating in a quasiballistic regime, our double-gated heterostructure allows a gate-defined p-n-p cavity to be formed and clear weak antilocalization (WAL) features to be shown consistent with Rashba-type SOC. At lower hole densities, a transition to a pronounced weak-localization (WL) feature is observed, signaling transport through a single spin-split valence band. These findings–in agreement with calculations–provide direct spectroscopic evidence of a proximity-induced spin-split band in BLG and underscore the potential of BLG/TMD heterostructures for spintronics and spin-based quantum technologies.

DOI: 10.1103/783y-y4bs

Combining graphene with transition metal dichalcogenides (TMDs) allows one to enhance the weak intrinsic spin-orbit coupling (SOC) strength of graphene while maintaining its high carrier mobility [1–12]. This enhanced SOC enables potential applications such as spin valves [13–15], spin polarizers [16,17], or spin logic gates [18, 19]. However, the limited tunability of the proximity-induced SOC in graphene-TMD heterobilayers makes it hard to tune such spin-based devices and remains a key challenge for the realization of graphene-based spin transistors [13,20]. In contrast, double-gated Bernal-stacked bilayer graphene (BLG) proximitized to a TMD is expected to exhibit gate-tunable SOC over a wide range [13,20].

*Contact author: bernd.beschoten@physik.rwth-aachen.de

The SOC tuning in BLG-TMD heterostructures relies on the tunable band gap of BLG under an applied out-of-plane displacement field [21,22]. As in gapped BLG at low charge-carrier density, electrons and holes are hosted on distinct graphene layers [13,20,23–27], and since proximity-induced SOC acts only on the layer in direct contact with the TMD [i.e., the proximal layer L1 in Fig. 1(a)], either the conduction or the valence band is spin-split depending on the direction of the applied electric displacement field [13,20], see the example in Fig. 1(b). A double-gated device geometry, incorporating both top and bottom gates [as schematically shown in Fig. 1(a)], enables independent control of the Fermi level μ_F and the band gap E_g, thereby allowing charge carriers to be shifted between layers with strong and weak SOC. This tunability forms the fundamental operating principle of a spin-orbit valve, which has been studied both theoretically [13,20] and experimentally [25,28].

Proximity-induced SOC in BLG also affects the Berry phase accumulated when encircling one of the K points in the Brillouin zone. In pristine BLG with negligible SOC, the Berry phase is $\pm 2\pi$, which leads to the observation of

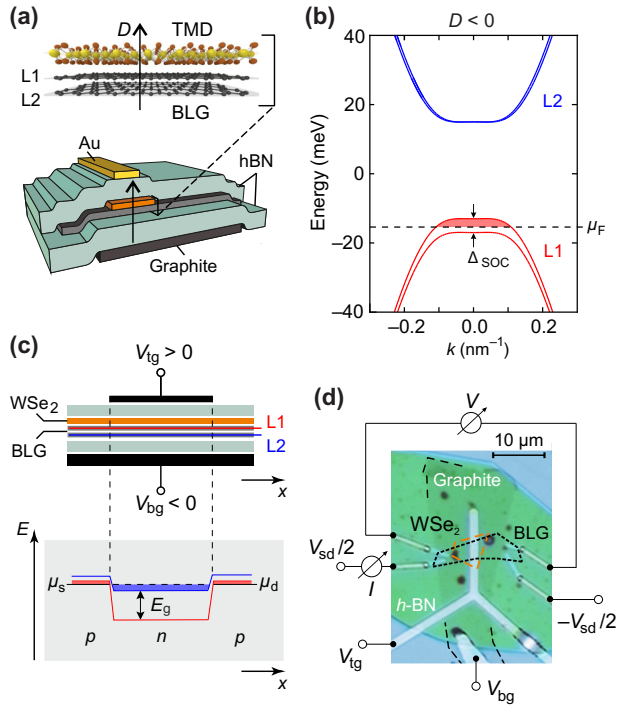

FIG. 1. (a) Schematics of the dual-gated BLG/TMD device. (b) Calculated band structure of BLG proximity coupled to WSe_2 for a negative displacement field D/ε_0. In this case, the valance band is spin split by Δ_{SOC}. (c) Schematic cross section of the device highlighting the proximal layer (L1) and the second graphene layer of the BLG (L2). The top gate allows the tuning of the Fermi level independently of the applied D field. For $V_{bg} < 0$, there will be hole (p) doping of the BLG regions that are not covered by the top gate. Positive top gate voltages ($V_{tg} > 0$) can create an n-doped region underneath the top gate, leading to the formation of lateral p-n junctions at the boundaries of the top gate (depicted in the lower panel). (d) False color image of the sample highlighting the different layered materials and electrical contacts of the device including the measurement scheme.

weak localization (WL) in diffusive, phase-coherent quantum transport [29–31]. In contrast, when Rashba-type SOC is induced–for example, via proximity to a TMD such as WSe_2–the Berry phase is reduced to $\pm\pi$ [32], resulting in weak antilocalization (WAL) [3–8,28,33–35]. The appearance of WAL is, in fact, commonly regarded as a hallmark of proximity-induced SOC in BLG-based heterostructures. The situation becomes more complex when a band gap is opened, as the accumulated Berry phase then depends on the k values that define the closed orbit. However, for orbits near the band edge, i.e., the K points, the accumulated Berry phase approaches zero, with its detailed dependence determined by the specifics of the proximity-induced SOC and the spin-split band structure. This gives rise to pronounced WL near the band edge, making it a sensitive probe for band-structure properties.

In this work, we report on a high-quality BLG/WSe_2 device that exhibits both high charge-carrier mobility and excellent band-gap tunability–indicative of minimal interfacial disorder. The device operates in a quasiballistic transport regime at a base temperature of 60 mK. We demonstrate that the electrostatic control enables the formation of gate-defined lateral p-n-p cavities, which give rise to phase-coherent transport features, including weak antilocalization, in the magnetoconductance. Furthermore, we observe pronounced weak localization that can be unambiguously attributed to the proximity-induced spin-split valence band of the graphene layer in contact with WSe_2. This provides direct evidence of the proximity-induced spin splitting probed by transport spectroscopy.

The device consists of a heterostructure of BLG/WSe_2 encapsulated between two crystals of hexagonal boron nitride (h-BN) equipped with a bottom gate made of graphite (Gr) and a narrow top gate made of gold [see schematic in Fig. 1(a), Raman spectra of the layered stack in Sec. I within the Supplemental Material [36] and Refs. [37–40] therein]. The graphite gate screens the disorder potential from the underlying SiO_2 substrate, allowing the opening of a clean band gap in BLG [41]. Flakes are selected by an automated flake search tool, where the thickness of the WSe_2 flakes is determined via their optical contrast [42,43]. Since the lateral size of the top gate is smaller than the bottom gate, only part of the BLG/WSe_2 heterostructure is double gated, while the remaining parts–which in the following will be called "leads"–are only tuned by the bottom gate, see Figs. 1(c) and 1(d). This allows the realization of electrostatically induced p-n junctions at the boundaries of the top-gated region in transport direction. For instance, the voltage configuration indicated in the schematics of Fig. 1(c) corresponds to a situation where the leads are p-doped while the double-gated region is n doped and has a band gap E_g induced by the electric displacement field.

The low-temperature, two-terminal resistance of such a device as a function of the voltages applied to the top and bottom gate, V_{tg} and V_{bg}, is shown in Fig. 2(a). The diagonal feature of elevated resistance indicates the shift of the midgap energy of the BLG in the double-gated region as a function of V_{tg} and V_{bg}, while the vertical feature at $V_{bg} = -0.12$ V originates from the charge neutrality point of the BLG regions that are only tuned by the back gate. The broadening of the diagonal high-resistance feature with increasing V_{tg} and V_{bg} indicates the opening of a band gap in the double-gated BLG region [41]. It is convenient to introduce the electric displacement field D in the double gated region, $D/\varepsilon_0 = e\,\alpha_{bg}[(V_{bg} - V_{bg}^0) - \beta(V_{tg} - V_{tg}^0)]/2$, and the effective gate voltage $V_g = [(V_{bg} - V_{bg}^0) + \beta(V_{tg} - V_{tg}^0)]/(1+\beta)$, where $\beta = \alpha_{tg}/\alpha_{bg}$ is the relative lever arm of the top and bottom gate, α_{tg} the top-gate lever arm, V_{tg}^0 and V_{bg}^0 account for the residual extrinsic doping

of the BLG, and e and ε_0 are the elementary charge and the vacuum permittivity, respectively [41]. For the device shown in Fig. 1(d), the relative lever-arm is $\beta = 1.34$, which corresponds to the (negative) slope of the diagonal line of high resistance in Fig. 2(a), while $\alpha_{tg} = 5.9 \times 10^{11}$ V^{-1} cm^{-2} is extracted from quantum Hall measurements (see Sec. II within the Supplemental Material [36] and Refs. [44–47] therein). By plotting the resistance in terms of D and V_g [see Fig. 2(b)], it becomes apparent that the width of the high-resistance region increases linearly with $|D|$, as expected from the opening of a band gap in BLG [see black dashed lines in Fig. 2(b)] [41].

The resistance data furthermore present a distinct asymmetry with respect to V_g [see also line traces in Fig. 2(d)], which can be attributed to the formation of lateral p-n junctions at the position of the edges of the top gate, depending on the value of V_g and D. For instance, for the case of Fig. 2(d) ($D < 0$), the region of low resistance for $V_g < 0$ corresponds to the situation in which the Fermi level, μ_F, is in the valence band of both the leads and of the double-gated central region; increasing V_g, μ_F enters the band gap of the double-gated region, which leads to a sharp increase of resistance of almost 4 orders of magnitude. For even larger values of V_g, μ_F enters the conduction band of the double-gated region, resulting in the formation of a p-n-p cavity. The resistance drops but remains significantly higher than for negative voltages due to the enhanced dwell times of the charge carriers in the cavity itself. The same behavior is observed for $D > 0$ and $V_g < 0$, with the formation of a n-p-n junction (see Sec. III within the Supplemental Material [36]).

The asymmetry with respect to V_g is also observed in the finite-bias spectroscopy measurements presented in Fig. 2(c). In this type of measurement, the appearance of a diamond-shaped region of suppressed conductance is the hallmark of the opening of a clean band gap in BLG [41,48]. The edges of the region of suppressed conductance correspond to the situation in which the electrochemical potential in the leads is aligned with the band edges in the double-gated region [41,48]. For perfectly clean band gaps, the edges of the diamond region are expected to have a slope of two. For the device of Fig. 1(d), the diamond shape is most pronounced at large displacement fields, where the slope of the outer edges reaches values of $\Delta V_{sd}/\Delta V_g = 1.9$ for the valence-band edge. This small deviation might be attributed to the presence of defects and trap states in the WSe_2 layer. The presence of defect or subgap states in the WSe_2 would also account for the observation that the maximum resistance measured in this type of device is about 2 orders of magnitude smaller than that observed in BLG/h-BN devices with graphite gates but without the WSe_2 layer, where resistance values as high as 100 GΩ have been reported [41]. Hopping transport through the trap states in WSe_2 would, indeed, represent a parallel conduction channel and lower the overall maximum resistance of the BLG/WSe_2 device compared to BLG/h-BN devices.

The finite-bias spectroscopy measurements in Fig. 2(c) serve as a direct probe of the magnitude of the electrostatically induced band gap in BLG, E_g, which is directly proportional to the maximal extension of the diamond along the V_{sd} axis. In Fig. 2(e), we show the respective value of E_g for both positive (full symbols) and negative (empty symbols) displacement fields. While the measured values of E_g are offset by about approximately 12 meV from what is theoretically predicted for BLG (dashed gray line), the data indicate a good band gap tunability in the BLG/WSe_2 heterostructure. The offset can be attributed to residual disorder [41], but may also originate partially from SOC-induced spin-split bands [13].

The good tunability of the band gap, E_g, is a strong indication of low disorder in the heterostructure [41], which is also reflected by the high charge-carrier mobility. For the device of Fig. 1(d) we extract $\mu_e \approx 260\,000$ cm^2 V^{-1} s^{-1} for electron transport at $T = 60$ mK (see Sec. IV within the Supplemental Material [36]). This results in a mean free path $l_m \approx 1.0 - 2.0$ μm, which is comparable with the length (i.e., the lateral extent in the transport direction) of the top gate, $l = 2$ μm, implying the device is in a quasiballistic transport regime.

To probe the proximity-induced SOC in BLG, we next discuss magnetoconductance measurements as a function of V_g for different values of the applied displacement field. In diffusive samples, it has been shown that the proximity-induced SOC results in the appearance of a weak antilocalization peak at low magnetic field [4,33,34]. Since our sample is quasiballistic, we expect to observe WAL more pronounced in gate configurations that correspond to the formation of a p-n-p cavity (i.e., for $D < 0$ and $V_g > 0$), or of a n-p-n cavity (i.e., for $D > 0$ and $V_g < 0$), where quantum interference effects can arise due to internal reflections at the p-n junctions, which results in extended dwell times.

Magnetotransport measurements at different values of the applied displacement field are presented in Fig. 3 for $D < 0$. Around $V_g \approx 0$ V, the conductance is strongly suppressed and does not depend on B, indicating that the Fermi level (μ_F) is in the band gap of the double-gated region. Outside this gap region, we observe a complicated pattern of universal conductance fluctuations (see Sec. V within the Supplemental Material [36] and Refs. [7,51,53] therein) as well as the emergence of a WAL peak at positive V_g, when μ_F is in the conduction band of the double-gated region forming a p-n-p cavity. This feature is best visualized by averaging different conductance traces measured over a range of gate voltages V_g, see Fig. 3(d). The respective gate voltage ranges are indicated by white boxes for the different displacement fields in Figs. 3(a)–3(c). Interestingly, WAL appears to be most clearly developed at large displacement fields $|D|$ (see Sec. VI within the Supplemental Material [36]), which may

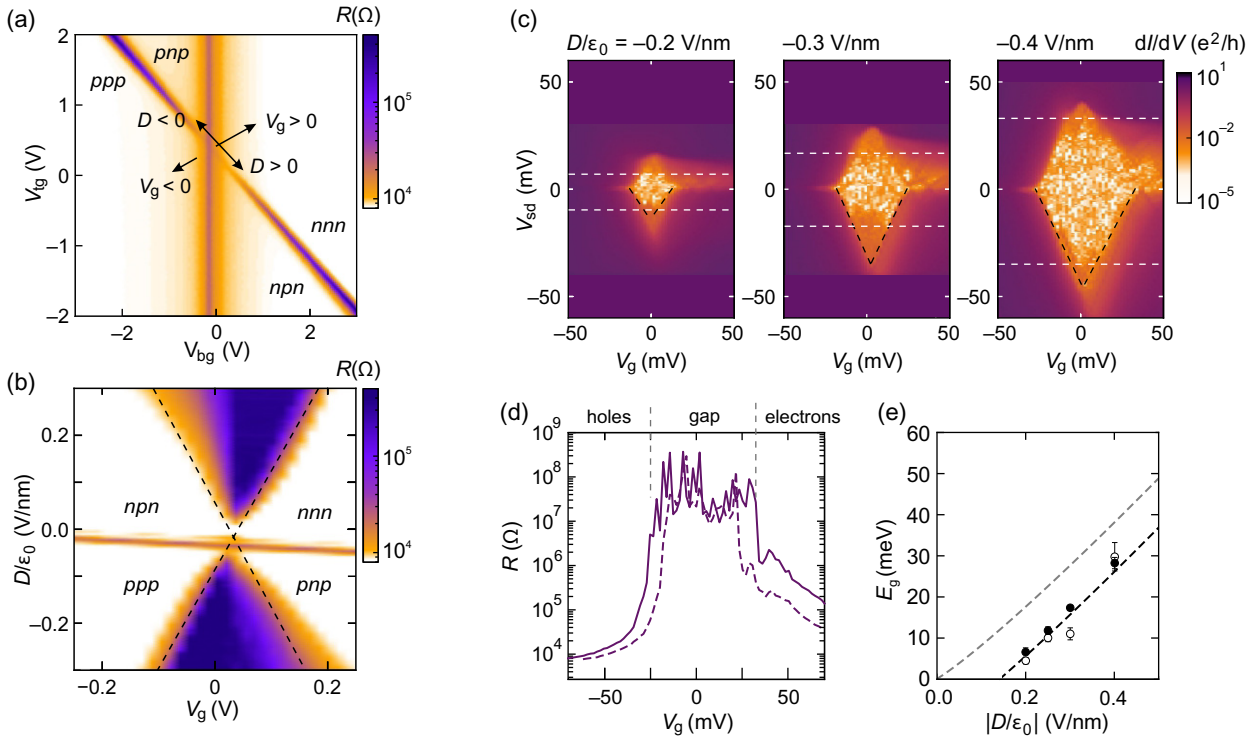

FIG. 2. (a) Two-terminal resistance of BLG/WSe_2 device as a function of top gate and bottom gate voltages ($V_{tg,bg}$). (b) Resistance as a function of the effective gate voltage V_g and of the electric displacement field D/ε_0 in the double-gated region. The measurements were from two different cooldowns and were performed at $T = 60$ mK, applying a small source-drain voltage of $V_{sd} = 1$ mV. (c) Finite bias spectroscopy measurements of the BLG/WSe_2 device showing the differential conductance as a function of V_{sd} and V_g for $D/\varepsilon_0 = -0.2, -0.3$, and -0.4 V/nm. The outline of the diamonds is highlighted by black dashed lines (assuming a threshold value of $dI/dV_{th} = 10^{-3}e^2/h$). The white dashed lines indicate the maximal extension of the diamond along the V_{sd} axis. (d) Line cuts through finite bias spectroscopy measurements at $V_{sd} = 1.5$ mV for displacement fields $D/\varepsilon_0 = -0.2$ V/nm (dashed purple) and $D/\varepsilon_0 = -0.4$ V/nm (solid purple) of the BLG/WSe_2 device. (e) Band-gap energies E_g of BLG extracted from finite bias spectroscopy for positive (filled circles) and negative (open circles) displacement fields [indicated with white dashed lines in (a)]. The orange line shows a theoretical prediction of E_g according to Ref. [21]. For the purple line, an offset of 12 meV was subtracted.

suggest that the *p*-*n*-*p* cavity plays a key role. From the width of the WAL peaks, we can estimate the phase coherence length [49,52], obtaining $l_\phi \approx \sqrt{h/(2e\Delta B_{FWHM})} \approx 3$ μm, which fulfills $l_\phi \gtrapprox l_m$, the condition for observing quantum interference effects [53].

The most remarkable feature of the data of Fig. 3 is, however, the existence of a narrow and sharply defined range of V_g at the top of the valence band, where the conductance exhibits a pronounced weak localization dip [see orange and red arrows in Figs. 3(b) and 3(c)]. The amplitude and the width of the WL signal exceeds those of the WAL signals by up to an order of magnitude [Fig. 3(e)]. We attribute this WL signal to transport through a single spin-polarized band in the double-gated region, which in turn results from the splitting of the valence band in BLG due to proximity-induced SOC. It has been shown, both in experiment [25] and theory [13,20], that proximity-induced SOC leads to a spin-split valence band for $D < 0$, as sketched in Fig. 1(b). In our device, the spin splitting leads near the band edge to a conductance mismatch between the central double-gated region and the adjacent BLG regions, enhancing the dwell time in the double-gated region and giving rise to a more pronounced WL signal. Therefore, the range of V_g in which WL can be observed is directly related to the band splitting induced by SOC, Δ_{SOC}. By converting the V_g range where we observe WL into a corresponding energy shift, we roughly estimate $\Delta_{SOC} \approx 2$ meV for $D/\varepsilon_0 = -0.3$ V/nm and $\Delta_{SOC} \approx 3$ meV for $D/\varepsilon_0 = -0.4$ V/nm (Sec. VII within the Supplemental Material [36]). These values are consistent with theoretical predictions [13,20,54,55] and experimental data of proximity-induced band splitting [24,25].

To interpret our experimental findings, it is crucial to consider the nature of carrier transport near the band edge of proximity-coupled gapped BLG. In this regime, the mean free path is significantly reduced due to two main factors: (i) enhanced scattering from impurity states and disorder introduced by the adjacent WSe_2 layer, and (ii) the relatively low Fermi velocity v_F (or, in other terms, the

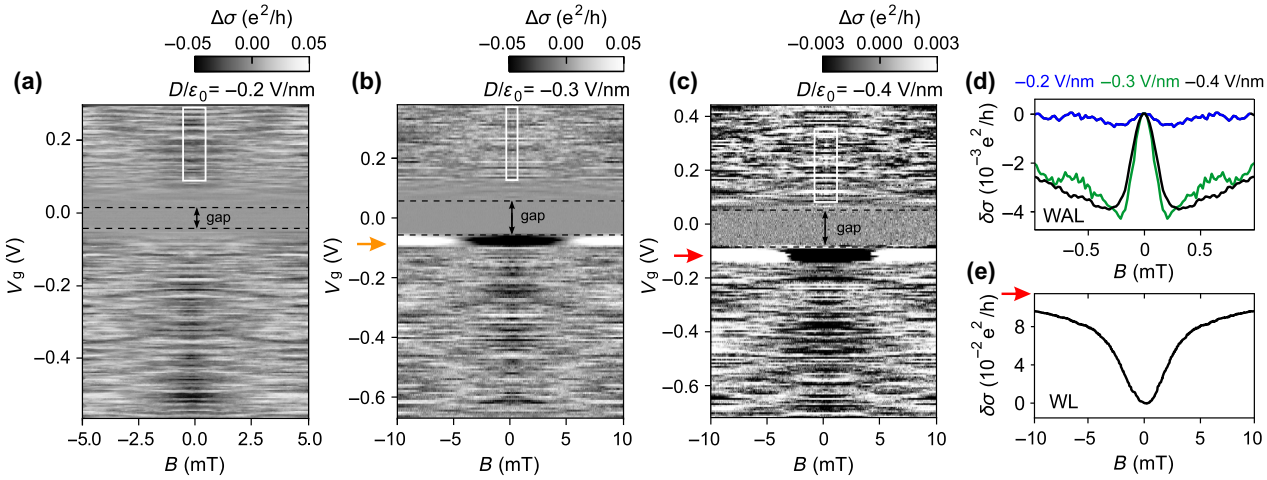

FIG. 3. Conductance as a function of V_g and B for different values of the displacement field: (a) $D/\varepsilon_0 = -0.2$ V/nm, (b) $D/\varepsilon_0 = -0.3$ V/nm, and (c) $D/\varepsilon_0 = -0.4$ V/nm. For better visualization, we plot the conductance $\Delta\sigma = \sigma(B, V_g = \text{const.}) - \langle\sigma(B, V_g = \text{const.})\rangle$ for each value of V_g, where we subtract the average over B of the measured conductance. (d) WAL peak for different values of D/ε_0. Here we plot $\delta\sigma = \Delta\sigma - \Delta\sigma(B = 0)$, averaged over the range of V_g indicated by the white boxes in (a), (b), and (c). (e) WL measured at $D/\epsilon_0 = -0.4$ V/nm and $V_g = -97$ mV. The WL signal is clearly visible at the top of the BLG valence band in (b) and (c) even without averaging over different gate voltages (see orange and red arrows).

high effective mass) near the band edge of gapped BLG. Both effects drive the system into a more diffusive transport regime. In addition, we note that the band mismatch between the double-gated BLG region (with one valence band) and the lead regions (with two valence bands) may also create an effective cavity, which increases the dwell time and thereby enhances the WL signal.

Of note, the observed WL signatures near the valence-band edge–where only one valence band is relevant–are consistent with expectations based on Berry-phase considerations. In Figs. 4(a) and 4(b) we show calculations of the band structure of the proximity-coupled WSe_2/BLG system for different SOC strength and the corresponding accumulated Berry phase for circles around the K point (for details see Secs. VIII and IX within the Supplemental Material [36] and Refs. [2,16,56] therein). To adjust the band gap and valence-band spin splitting, we choose a layer potential difference of 15 meV and a valley-Zeeman spin-orbit coupling (SOC) strength of $\lambda_{VZ} = 2$ meV, which is in line with the results of earlier experiments [7,28] and theoretical expectations [2,13,57]. The different panels of Figs. 4(a) and 4(b) correspond to different strengths of Rashba SOC, namely $\lambda_R = \lambda_{VZ}/5$, $\lambda_R = \lambda_{VZ}$, and $\lambda_R = 5\lambda_{VZ}$ from left to right. In Fig. 4(a), we see that independent of the Rashba SOC strength, the valence band is always strongly spin polarized along the z axis (out-of-plane direction) near the band edge. In Fig. 4(b), we plot [corresponding to the panels in Fig. 4(a)] the accumulated Berry phase as a function of the integration radius k (for more information on the calculations see Sec. IX within the Supplemental Material [36] and Refs. [50,58] therein). Crucially, the resulting Berry phase is always close to 0 near the band edge (i.e., K point), giving rise to a pronounced WL instead of a WAL signal when only the upper valence band is occupied [50]. This finding is independent of the relative Rashba and valley-Zeeman strength and is consistent with our measurements. The same argumentation holds for the K' point without a loss of generality except for a sign change of the Berry phase for increasing k.

Having established that the WL signal is consistent with band-structure calculations, we now examine how the WL signal evolves with the hole density. As shown in Fig. 4(c), the amplitude of the WL signal rises sharply at low hole densities near the top of the valence band, peaks at $n = -0.35 \times 10^{11}$ cm^{-2}, and then decreases again at higher hole densities. We model this behavior by considering a general expression for WL and WAL in BLG [28] (for more details on the model, see Sec. X within the Supplemental Material [36] and Refs. [28,59] therein). The scattering parameters are estimated based on the cavity dimensions, the diffusion constant, and the Fermi velocity $v_F(n)$, which we extract from band-structure calculations. Figure 4(d) shows calculated WL curves for carrier densities in the range of -0.14 to -0.49×10^{11} cm^{-2} based on the scattering model. At lower carrier densities, the increasing WL amplitude with hole density matches well the experimental trend in Fig. 4(c). Since our model includes only the upper valence band, the calculated WL amplitude increases with hole density across the entire range. In contrast, the measured WL amplitude drops sharply when the second valence band is populated [see dashed curves in Fig. 4(c)]. We attribute this to spin precession and spin-mixing effects that can appear when two

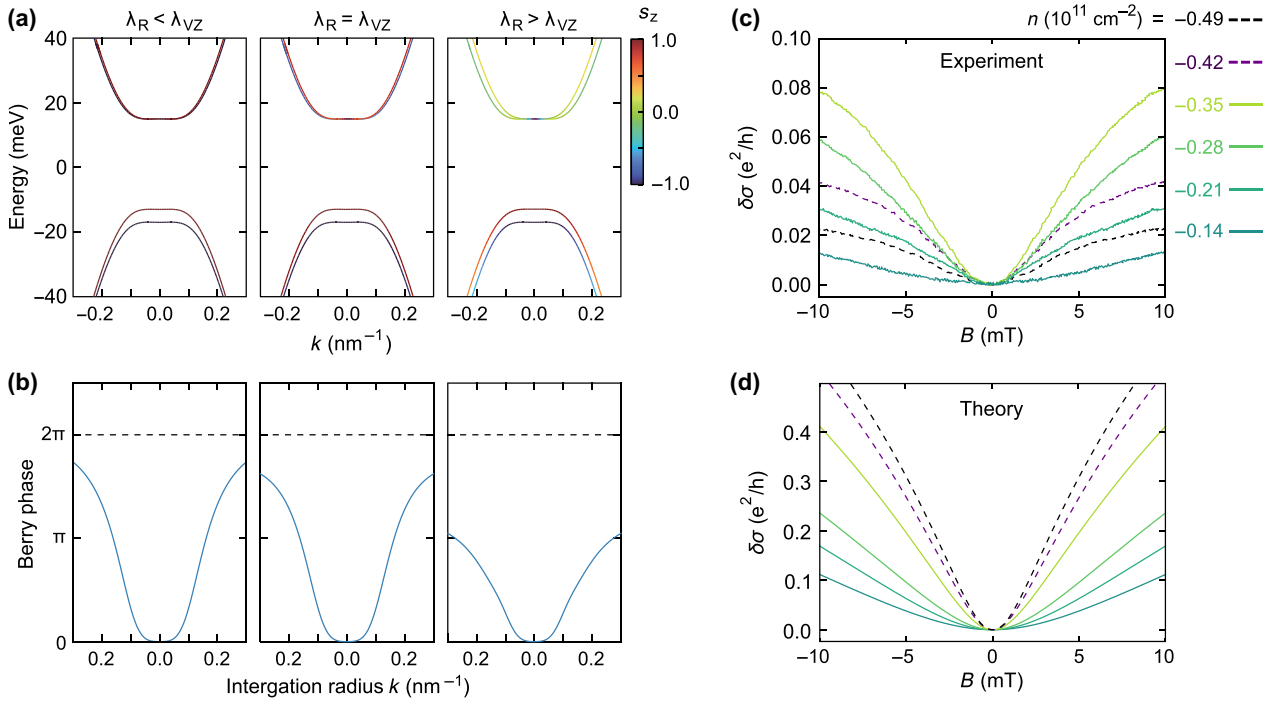

FIG. 4. (a) Calculated low-energy bands of a BLG/WSe_2 heterostructure for different ratios between the Rashba SOC strength λ_R and the Valley-Zeeman SOC strength λ_{VZ} at the K point ($\tau = 1$). The color scale denotes the out-of-plane spin orientation. (b) The corresponding Berry phase of the highest spin-split valence band, calculated around a closed contour in reciprocal space at a fixed momentum magnitude k with the center being the K point. Close to the band edge, the Berry phase is zero for the upper valence band, suggesting that WAL is completely suppressed when only one band is occupied [4,33,49,50]. Further into the band, the Berry phase approaches 2π if $\lambda_R < \lambda_{VZ}$, or if $\lambda_R = \lambda_{VZ}$, and approaches π if $\lambda_R > \lambda_{VZ}$. This behavior is seen at the K' point except for a sign switch in the Berry phase. (c) Normalized magnetoconductance $\delta\sigma$ extracted from a ΔV_g regime close to the valence-band edge [see orange outline in Fig. 3(b)]. (d) Calculated WL signal within the spin-split bands, assuming that scattering and spin relaxation only occur at the edges of the top-gate-defined cavity and the BLG. The results show that for increasing hole density $|n|$ the width of the WL decreases, which is consistent with our measurements for $n \in [-0.14, -0.35] \times 10^{11}$ cm^{-2}. For higher $|n|$, we get contributions from the other spin-split band, resulting in a suppression of the WL signal.

bands are occupied, opening up additional spin-relaxation channels that will reduce the spin lifetime and the magnitude of the WL curves. This trend of reduced WL with reduced spin lifetime is shown in Sec. X within the Supplemental Material [36]. Note that at low hole densities, both experiment and simulation show a clear broadening of the WL curves. Our model attributes this to a reduced diffusion coefficient, which scales with $v_F^2/2$ and thus decreases with lowering hole density.

In summary, we have presented a double-gated BLG/WSe_2 heterostructure that combines high mobility, excellent electrostatic control, and clear signatures of proximity-induced spin-orbit coupling in phase-coherent transport. The use of graphite gates enables clean and tunable band gaps, almost comparable to those in pristine BLG, and allows full access to both conduction and valence bands. Notably, no screening effects from the WSe_2 layer are observed, indicating a well-behaved interface.

Magnetotransport measurements reveal a transition from weak antilocalization to weak localization as the Fermi level is tuned into the upper valence band. This behavior is consistent with theoretical expectations: near the band edge, the Berry phase drops towards zero, independent of the relative strength of Rashba and valley-Zeeman spin-orbit coupling. The observed trends in the WL amplitude as a function of hole density are captured by a scattering model, using input parameters derived from band-structure calculations. Taken together, these findings provide spectroscopic evidence for proximity-induced spin split bands in BLG, probed by phase-coherent transport. The combination of low disorder, sharp band edges, and precise gate control establishes a robust platform for spin-sensitive mesoscopic devices. Therefore, such systems open the door to exploring gate-defined quantum point contacts, spin filters, and quantum dots in bilayer graphene with tunable spin-orbit coupling, as also demonstrated recently [60,61].

ACKNOWLEDGMENTS

The authors thank S. Trellenkamp, F. Lentz, and D. Neumaier for their support in device fabrication. We also

thank J. Eroms, J. Amann, and J. Fabian for discussions about the nature of WAL, K. Zollner for discussions about proximity effects in BLG on WSe_2, and F. Haupt for help on the manuscript. This project has received funding from the European Union's Horizon 2020 research and innovation programme under Grant Agreement No. 881603 (Graphene Flagship) and from the European Research Council (ERC) under Grant Agreement No. 820254, the Deutsche Forschungsgemeinschaft (DFG, German Research Foundation) under Germany's Excellence Strategy - Cluster of Excellence Matter and Light for Quantum Computing (ML4Q) EXC 2004/1 - 390534769 and by the Helmholtz Nano Facility [62]. K.W. and T.T. acknowledge support from the JSPS KAKENHI (Grants No. 21H05233 and No. 23H02052) and World Premier International Research Center Initiative (WPI), MEXT, Japan. ICN2 is funded by the CERCA programme / Generalitat de Catalunya, and is supported by the Severo Ochoa Centres of Excellence programme, Grant No. CEX2021-001214-S, funded by MCIN/AEI/10.13039.501100011033.

DATA AVAILABILITY

The data that support the findings of this article are openly available [63].

[1] M. Gmitra and J. Fabian, Graphene on transition-metal dichalcogenides: A platform for proximity spin-orbit physics and optospintronics, Phys. Rev. B **92**, 155403 (2015).

[2] M. Gmitra, D. Kochan, P. Högl, and J. Fabian, Trivial and inverted dirac bands and the emergence of quantum spin hall states in graphene on transition-metal dichalcogenides, Phys. Rev. B **93**, 155104 (2016).

[3] Z. Wang, D.-K. Ki, H. Chen, H. Berger, A. H. MacDonald, and A. F. Morpurgo, Strong interface-induced spin–orbit interaction in graphene on WS_2, Nat. Commun. **6**, 8339 (2015).

[4] Z. Wang, D.-K. Ki, J. Y. Khoo, D. Mauro, H. Berger, L. S. Levitov, and A. F. Morpurgo, Origin and magnitude of "designer" spin-orbit interaction in graphene on semiconducting transition metal dichalcogenides, Phys. Rev. X **6**, 041020 (2016).

[5] B. Yang, M. Lohmann, D. Barroso, I. Liao, Z. Lin, Y. Liu, L. Bartels, K. Watanabe, T. Taniguchi, and J. Shi, Strong electron-hole symmetric Rashba spin-orbit coupling in graphene/monolayer transition metal dichalcogenide heterostructures, Phys. Rev. B **96**, 041409(R) (2017).

[6] T. Völkl, T. Rockinger, M. Drienovsky, K. Watanabe, T. Taniguchi, D. Weiss, and J. Eroms, Magnetotransport in heterostructures of transition metal dichalcogenides and graphene, Phys. Rev. B **96**, 125405 (2017).

[7] S. Zihlmann, A. W. Cummings, J. H. Garcia, M. Kedves, K. Watanabe, T. Taniguchi, C. Schönenberger, and P. Makk, Large spin relaxation anisotropy and valley-Zeeman spin-orbit coupling in WSe_2/graphene/*h*-BN heterostructures, Phys. Rev. B **97**, 075434 (2018).

[8] T. Wakamura, F. Reale, P. Palczynski, S. Guéron, C. Mattevi, and H. Bouchiat, Strong anisotropic spin-orbit interaction induced in graphene by monolayer WS_2, Phys. Rev. Lett. **120**, 106802 (2018).

[9] L. Banszerus, T. Sohier, A. Epping, F. Winkler, F. Libisch, F. Haupt, K. Watanabe, T. Taniguchi, K. Mü-Caspary, N. Marzari, F. Mauri, B. Beschoten, and C. Stampfer, Extraordinary high room-temperature carrier mobility in graphene-WSe_2 heterostructures, arXiv:1909.09523.

[10] B. Füöp, A. Márffy, S. Zihlmann, M. Gmitra, E. Tóvári, B. Szentpéteri, M. Kedves, K. Watanabe, T. Taniguchi, J. Fabian, C. Schönenberger, P. Makk, and S. Csonka, Boosting proximity spin–orbit coupling in graphene/WSe_2 heterostructures via hydrostatic pressure, npj 2D Mater. Appl. **5**, 1 (2021).

[11] P. Tiwari, M. K. Jat, A. Udupa, D. S. Narang, K. Watanabe, T. Taniguchi, D. Sen, and A. Bid, Experimental observation of spin-split energy dispersion in high-mobility single-layer graphene/WSe_2 heterostructures, npj 2D Mater. Appl. **6**, 68 (2022).

[12] T. Bisswanger, A. Schmidt, F. Volmer, C. Stampfer, and B. Beschoten, Room-temperature spin-lifetime anisotropy exceeding 60 in bilayer graphene spin valves proximity coupled to WSe_2, 2D Mater. **13**, 015025 (2026).

[13] M. Gmitra and J. Fabian, Proximity effects in bilayer graphene on monolayer WSe_2: Field-effect spin valley locking, spin-orbit valve, and spin transistor, Phys. Rev. Lett. **119**, 146401 (2017).

[14] J. H. Garcia, M. Vila, A. W. Cummings, and S. Roche, Spin transport in graphene/transition metal dichalcogenide heterostructures, Chem. Soc. Rev. **47**, 3359 (2018).

[15] E. C. Ahn, 2D materials for spintronic devices, npj 2D Mater. Appl. **4**, 17 (2007).

[16] A. W. Cummings, J. H. Garcia, J. Fabian, and S. Roche, Giant spin lifetime anisotropy in graphene induced by proximity effects, Phys. Rev. Lett. **119**, 206601 (2017).

[17] J. Ingla-Aynés, F. Herling, J. Fabian, L. E. Hueso, and F. Casanova, Electrical control of valley-Zeeman spin-orbit-coupling–induced spin precession at room temperature, Phys. Rev. Lett. **127**, 047202 (2021).

[18] W. Han, R. K. Kawakami, M. Gmitra, and J. Fabian, Graphene spintronics, Nat. Nanotechnol. **9**, 794 (2014).

[19] G. Hu and B. Xiang, Recent advances in two-dimensional spintronics, Nanoscale Res. Lett. **15**, 1556 (2020).

[20] J. Y. Khoo, A. F. Morpurgo, and L. Levitov, On-demand spin orbit interaction from which-layer tunability in bilayer graphene, Nano Lett. **17**, 7003 (2017).

[21] E. McCann and M. Koshino, The electronic properties of bilayer graphene, Rep. Prog. Phys. **76**, 056503 (2013).

[22] S. Slizovskiy, A. Garcia-Ruiz, A. I. Berdyugin, N. Xin, T. Taniguchi, K. Watanabe, A. K. Geim, N. D. Drummond, and V. I. Fal'ko, Out-of-plane dielectric susceptibility of graphene in twistronic and Bernal bilayers, Nano Lett. **21**, 6678 (2021).

[23] A. F. Young and L. S. Levitov, Capacitance of graphene bilayer as a probe of layer-specific properties, Phys. Rev. B **84**, 085441 (2011).

[24] D. Wang, S. Che, G. Cao, R. Lyu, K. Watanabe, T. Taniguchi, C. N. Lau, and M. Bockrath, Quantum Hall effect measurement of spin-orbit coupling strengths in ultraclean bilayer graphene/WSe_2 heterostructures, Nano Lett. **19**, 7028 (2019).

[25] J. O. Island, X. Cui, C. Lewandowski, J. Y. Khoo, E. M. Spanton, H. Zhou, D. Rhodes, J. C. Hone, T. Taniguchi, K. Watanabe, L. S. Levitov, M. P. Zaletel, and A. F. Young, Spin–orbit-driven band inversion in bilayer graphene by the van der Waals proximity effect, Nature **571**, 85 (2019).

[26] M. Masseroni, M. Gull, A. Panigrahi, N. Jacobsen, F. Fischer, C. Tong, J. D. Gerber, M. Niese, T. Taniguchi, K. Watanabe, L. Levitov, T. Ihn, K. Ensslin, and H. Duprez, Spin-orbit proximity in MoS_2/bilayer graphene heterostructures, Nat. Commun. **15**, 1 (2024).

[27] A. M. Seiler, Ya. Zhumagulov, K. Zollner, C. Yoon, D. Urbaniak, F. R. Geisenhof, K. Watanabe, T. Taniguchi, J. Fabian, F. Zhang, and R. T. Weitz, Layer-selective spin-orbit coupling and strong correlation in bilayer graphene, 2D Mater. **12**, 035009 (2025).

[28] J. Amann, T. Völkl, T. Rockinger, D. Kochan, K. Watanabe, T. Taniguchi, J. Fabian, D. Weiss, and J. Eroms, Counterintuitive gate dependence of weak antilocalization in bilayer graphene/WSe_2 heterostructures, Phys. Rev. B **105**, 115425 (2022).

[29] R. V. Gorbachev, F. V. Tikhonenko, A. S. Mayorov, D. W. Horsell, and A. K. Savchenko, Weak localization in bilayer graphene, Phys. Rev. Lett. **98**, 176805 (2007).

[30] Z.-M. Liao, B.-H. Han, H.-C. Wu, and D.-P. Yu, Gate voltage dependence of weak localization in bilayer graphene, Appl. Phys. Lett. **97**, 163110 (2010).

[31] S. Engels, B. Terrés, A. Epping, T. Khodkov, K. Watanabe, T. Taniguchi, B. Beschoten, and C. Stampfer, Limitations to carrier mobility and phase-coherent transport in bilayer graphene, Phys. Rev. Lett. **113**, 126801 (2014).

[32] X. Zhai, Layered opposite Rashba spin-orbit coupling in bilayer graphene: Loss of spin chirality, symmetry breaking, and topological transition, Phys. Rev. B **105**, 205429 (2022).

[33] B. Yang, M.-F. Tu, J. Kim, Y. Wu, H. Wang, J. Alicea, R. Wu, M. Bockrath, and J. Shi, Tunable spin–orbit coupling and symmetry-protected edge states in graphene/WS_2, 2D Mater. **3**, 031012 (2016).

[34] A. M. Afzal, M. F. Khan, G. Nazir, G. Dastgeer, S. Aftab, I. Akhtar, Y. Seo, and J. Eom, Gate modulation of the spin-orbit interaction in bilayer graphene encapsulated by WS_2 films, Sci. Rep. **8**, 3412 (2018).

[35] S. Jafarpisheh, A. W. Cummings, K. Watanabe, T. Taniguchi, B. Beschoten, and C. Stampfer, Proximity-induced spin-orbit coupling in graphene/$Bi_{1.5}Sb_{0.5}Te_{1.7}Se_{1.3}$ heterostructures, Phys. Rev. B **98**, 241402(R) (2018).

[36] See Supplemental Material at http://link.aps.org/supplemental/10.1103/783y-y4bs for Raman spectra; the determination of gate lever arms; complementary finite bias spectroscopy data; the determination of mobility, mean-free path and phase coherence length; magnetotransport measurements; an estimate of the spin splitting; the Hamiltonian of BLG/TMD; a calculation of the Berry phase; a weak localization model. The Supplemental Material also includes Refs. [2,7,16,28,37–40,44–47,50,51,53,56,58,59].

[37] E. del Corro, H. Terrones, A. Elias, C. Fantini, S. Feng, M. A. Nguyen, T. E. Mallouk, M. Terrones, and M. A. Pimenta, Excited excitonic states in 1L, 2L, 3L, and bulk WSe_2 observed by resonant Raman spectroscopy, ACS Nano **8**, 9629 (2014).

[38] D. Graf, F. Molitor, K. Ensslin, C. Stampfer, A. Jungen, C. Hierold, and L. Wirtz, Spatially resolved Raman spectroscopy of single- and few-layer graphene, Nano Lett. **7**, 238 (2007).

[39] C. Neumann, S. Reichardt, P. Venezuela, M. Drögeler, L. Banszerus, M. Schmitz, K. Watanabe, T. Taniguchi, F. Mauri, B. Beschoten, S. V. Rotkin, and C. Stampfer, Raman spectroscopy as probe of nanometre-scale strain variations in graphene., Nat. Commun. **6**, 8429 (2015).

[40] M. Schmitz, S. Engels, L. Banszerus, K. Watanabe, T. Taniguchi, C. Stampfer, and B. Beschoten, High mobility dry-transferred CVD bilayer graphene, Appl. Phys. Lett. **110**, 263110 (2017).

[41] E. Icking, L. Banszerus, F. Wörtche, F. Volmer, P. Schmidt, C. Steiner, S. Engels, J. Hesselmann, M. Goldsche, K. Watanabe, T. Taniguchi, C. Volk, B. Beschoten, and C. Stampfer, Transport spectroscopy of ultraclean tunable band gaps in bilayer graphene, Adv. Electron. Mater. **8**, 2200510 (2022).

[42] J.-L. Uslu, T. Ouaj, D. Tebbe, A. Nekrasov, J. H. Bertram, M. Schütte, K. Watanabe, T. Taniguchi, B. Beschoten, L. Waldecker, and C. Stampfer, An open-source robust machine learning platform for real-time detection and classification of 2D material flakes, Mach. Learn.: Sci. Technol. **5**, 015027 (2024).

[43] J.-L. Uslu, A. Nekrasov, A. Hermans, B. Beschoten, B. Leibe, L. Waldecker, and C. Stampfer, MaskTerial: A foundation model for automated 2D material flake detection, Digit. Discov. **4**, 3744 (2025).

[44] Y. Zhao, P. Cadden-Zimansky, Z. Jiang, and P. Kim, Symmetry breaking in the zero-energy landau level in bilayer graphene, Phys. Rev. Lett. **104**, 066801 (2010).

[45] J. Dauber, M. Oellers, F. Venn, A. Epping, K. Watanabe, T. Taniguchi, F. Hassler, and C. Stampfer, Aharonov-Bohm oscillations and magnetic focusing in ballistic graphene rings, Phys. Rev. B **96**, 205407 (2017).

[46] J. Sonntag, S. Reichardt, L. Wirtz, B. Beschoten, M. I. Katsnelson, F. Libisch, and C. Stampfer, Impact of many-body effects on Landau levels in graphene, Phys. Rev. Lett. **120**, 187701 (2018).

[47] M. Schmitz, T. Ouaj, Z. Winter, K. Rubi, K. Watanabe, T. Taniguchi, U. Zeitler, B. Beschoten, and C. Stampfer, Fractional quantum Hall effect in CVD-grown graphene, 2D Mater. **7**, 041007 (2020).

[48] E. Icking, D. Emmerich, K. Watanabe, T. Taniguchi, B. Beschoten, M. C. Lemme, J. Knoch, and C. Stampfer, Ultrasteep slope cryogenic FETs based on bilayer graphene, Nano Lett. **24**, 11454 (2024).

[49] K. Kechedzhi, E. McCann, V. I. Fal'ko, H. Suzuura, T. Ando, and B. L. Altshuler, Weak localization in monolayer and bilayer graphene, Eur. Phys. J. Spec. Top. **148**, 39 (2007).

[50] H.-Z. Lu, J. Shi, and S.-Q. Shen, Competition between weak localization and antilocalization in topological surface states, Phys. Rev. Lett. **107**, 076801 (2011).

[51] P. A. Lee, A. D. Stone, and H. Fukuyama, Universal conductance fluctuations in metals: Effects of finite temperature, interactions, and magnetic field, Phys. Rev. B **35**, 1039 (1987).

[52] S. Ilić, J. S. Meyer, and M. Houzet, Weak localization in transition metal dichalcogenide monolayers and their heterostructures with graphene, Phys. Rev. B **99**, 205407 (2019).

[53] H. Bluhm, T. Brückel, M. Morgenstern, G. von Plessen, and C. Stampfer, *Electrons in Solids: Mesoscopics, Photonics, Quantum Computing, Correlations, Topology* (De Gruyter, 2019).

[54] K. Zollner, M. Gmitra, and J. Fabian, Swapping exchange and spin-orbit coupling in 2D van der Waals heterostructures, Phys. Rev. Lett. **125**, 196402 (2020).

[55] K. Zollner and J. Fabian, Bilayer graphene encapsulated within monolayers of WS_2 or $Cr_2Ge_2Te_6$: Tunable proximity spin-orbit or exchange coupling, Phys. Rev. B **104**, 075126 (2021).

[56] J. Jung and A. H. MacDonald, Accurate tight-binding models for the π bands of bilayer graphene, Phys. Rev. B **89**, 035405 (2014).

[57] T. Naimer, K. Zollner, M. Gmitra, and J. Fabian, Twist-angle dependent proximity induced spin-orbit coupling in graphene/transition metal dichalcogenide heterostructures, Phys. Rev. B **104**, 195156 (2021).

[58] R. Resta, Macroscopic polarization in crystalline dielectrics: The geometric phase approach, Rev. Mod. Phys. **66**, 899 (1994).

[59] E. McCann and V. I. Fal'ko, $z \rightarrow -z$ symmetry of spin-orbit coupling and weak localization in graphene, Phys. Rev. Lett. **108**, 166606 (2012).

[60] H. Dulisch, D. Emmerich, E. Icking, K. Hecker, S. Möller, L. Müller, K. Watanabe, T. Taniguchi, C. Volk, and C. Stampfer, Electric-field-tunable spin–orbit gap in a bilayer graphene/WSe_2 quantum dot, Nano Lett. **25**, 10549 (2025).

[61] J. D. Gerber, E. Ersoy, M. Masseroni, M. Niese, M. Laumer, A. O. Denisov, H. Duprez, W. W. Huang, C. Adam, L. Ostertag, C. Tong, T. Taniguchi, K. Watanabe, V. I. Fal'ko, T. Ihn, K. Ensslin, and A. Knothe, Tunable spin–orbit splitting in bilayer graphene/WSe_2 quantum devices, Nano Lett. **25**, 12480 (2025).

[62] W. Albrecht, J. Moers, and B. Hermanns, HNF - Helmholtz Nano Facility, J. Large-Scale Res. Facil. **3**, A112 (2017).

[63] The data supporting the findings of this work are available in a Zenodo repository under. https://doi.org/10.5281/zenodo.15874609.